Cell Reports

Neuronal cholesterol synthesis is essential for repair of chronically demyelinated lesions in mice

Graphical abstract

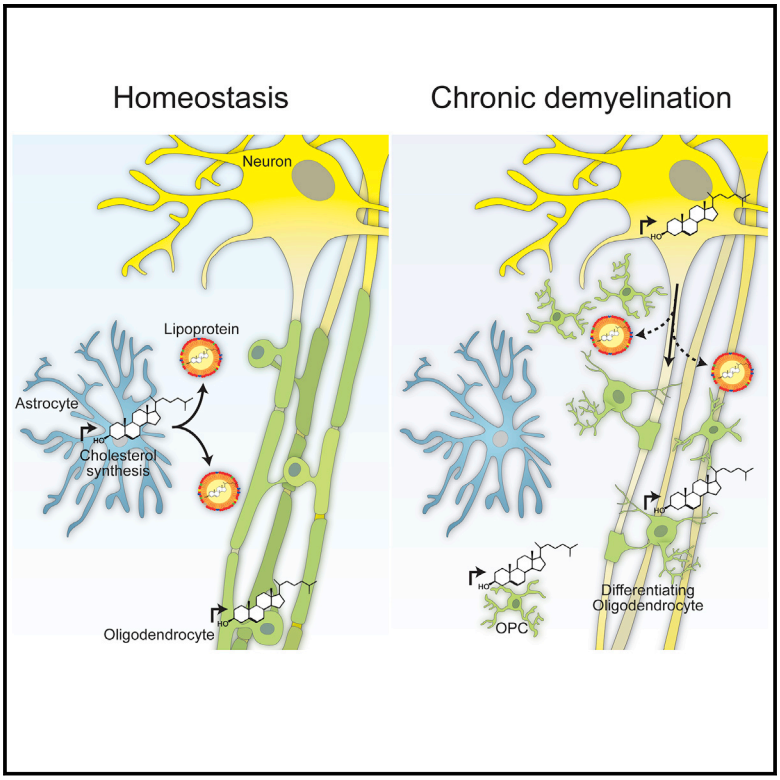

Authors

Stefan A. Berghoff, Lena Spieth, Ting Sun, ..., Till Ischebeck, Julia M. Edgar, Gesine Saher

Correspondence

berghoff@em.mpg.de (S.A.B.), saher@em.mpg.de (G.S.)

In brief

Endogenous repair after chronic demyelination requires local cholesterol synthesis. Berghoff et al. show that in addition to oligodendroglia, neurons upregulate cholesterol synthesis in mouse models and patients with MS. Neuronal cholesterol facilitates repair, especially by augmenting proliferation of oligodendrocyte precursor cells.

Highlights

- Neurons increase cholesterol synthesis in chronic myelin disease and multiple sclerosis
- Remyelination is facilitated by neuronal and oligodendroglial cholesterol synthesis
- Neuronal cholesterol augments proliferation of oligodendrocyte precursor cells

Berghoff et al., 2021, Cell Reports *37*, 109889
October 26, 2021 © 2021 The Author(s).
https://doi.org/10.1016/j.celrep.2021.109889

CellPress

Cell Reports

CellPress
OPEN ACCESS

Report

Neuronal cholesterol synthesis is essential for repair of chronically demyelinated lesions in mice

Stefan A. Berghoff,[1,10,*] Lena Spieth,[1,10] Ting Sun,[1,2,10] Leon Hosang,[3] Constanze Depp,[1] Andrew O. Sasmita,[1] Martina H. Vasileva,[1] Patricia Scholz,[4] Yu Zhao,[2] Dilja Krueger-Burg,[5] Sven Wichert,[6] Euan R. Brown,[7] Kyriakos Michail,[7] Klaus-Armin Nave,[1] Stefan Bonn,[2] Francesca Odoardi,[3] Moritz Rossner,[6] Till Ischebeck,[4,8] Julia M. Edgar,[1,9] and Gesine Saher[1,11,*]

[1]Department of Neurogenetics, Max Planck Institute of Experimental Medicine, Göttingen, Germany
[2]Institute for Medical Systems Biology, Center for Molecular Neurobiology Hamburg, Hamburg, Germany
[3]Institute for Neuroimmunology and Multiple Sclerosis Research, University Medical Center Göttingen, Göttingen, Germany
[4]Department of Plant Biochemistry, Albrecht-von-Haller-Institute for Plant Sciences and Göttingen Center for Molecular Biosciences (GZMB), University of Göttingen, Göttingen, Germany
[5]Department of Molecular Neurobiology, Max Planck Institute of Experimental Medicine, Göttingen, Germany
[6]Department of Psychiatry and Psychotherapy, University Hospital, LMU Munich, Munich, Germany
[7]School of Engineering and Physical Sciences, Institute of Biological Chemistry, Biophysics and Bioengineering, James Naysmith Building, Heriot Watt University, Edinburgh, UK
[8]Service Unit for Metabolomics and Lipidomics, Göttingen Center for Molecular Biosciences (GZMB), University of Göttingen, Göttingen, Germany
[9]Axo-glial Group, Institute of Infection, Immunity and Inflammation, College of Medical Veterinary and Life Sciences, University of Glasgow, Glasgow, UK
[10]These authors contributed equally
[11]Lead contact
*Correspondence: berghoff@em.mpg.de (S.A.B.), saher@em.mpg.de (G.S.)
https://doi.org/10.1016/j.celrep.2021.109889

SUMMARY

Astrocyte-derived cholesterol supports brain cells under physiological conditions. However, in demyelinating lesions, astrocytes downregulate cholesterol synthesis, and the cholesterol that is essential for remyelination has to originate from other cellular sources. Here, we show that repair following acute versus chronic demyelination involves distinct processes. In particular, in chronic myelin disease, when recycling of lipids is often defective, *de novo* neuronal cholesterol synthesis is critical for regeneration. By gene expression profiling, genetic loss-of-function experiments, and comprehensive phenotyping, we provide evidence that neurons increase cholesterol synthesis in chronic myelin disease models and in patients with multiple sclerosis (MS). In mouse models, neuronal cholesterol facilitates remyelination specifically by triggering oligodendrocyte precursor cell proliferation. Our data contribute to the understanding of disease progression and have implications for therapeutic strategies in patients with MS.

INTRODUCTION

During normal brain development, cholesterol is produced locally by *de novo* synthesis involving all CNS cells (Berghoff et al., 2021; Camargo et al., 2012; Fünfschilling et al., 2012). Neuronal cholesterol is essential during neurogenesis (Fünfschilling et al., 2012), but the highest rates of cholesterol synthesis in the brain are achieved by oligodendrocytes during post-natal myelination (Dietschy, 2009). The resulting cholesterol-rich myelin enwraps, shields, and insulates axons to enable rapid conduction of neuronal impulses. In the adult brain, cholesterol synthesis is attenuated to low steady-state levels (Dietschy and Turley, 2004).

Destruction of lipid-rich myelin in demyelinating diseases such as multiple sclerosis (MS) likely impairs neuronal function by disrupting the axon-myelin unit (Stassart et al., 2018). Remyelination is considered crucial for limiting axon damage and slowing progressive clinical disability. Statin-mediated inhibition of the cholesterol synthesis pathway impairs remyelination (Miron et al., 2009). Previously, we showed that following an acute demyelinating episode, oligodendrocytes import cholesterol for new myelin membranes from damaged myelin that has been recycled by phagocytic microglia (Berghoff et al., 2021). In contrast, oligodendroglial cholesterol synthesis contributes to remyelination following chronic demyelination (Berghoff et al., 2021; Voskuhl et al., 2019). Notably, astrocytes reduce expression of cholesterol synthesis genes following demyelination (Berghoff et al., 2021; Itoh et al., 2018). As in the healthy brain, astrocytes support neurons

This is an open access article under the CC BY-NC-ND license (http://creativecommons.org/licenses/by-nc-nd/4.0/).

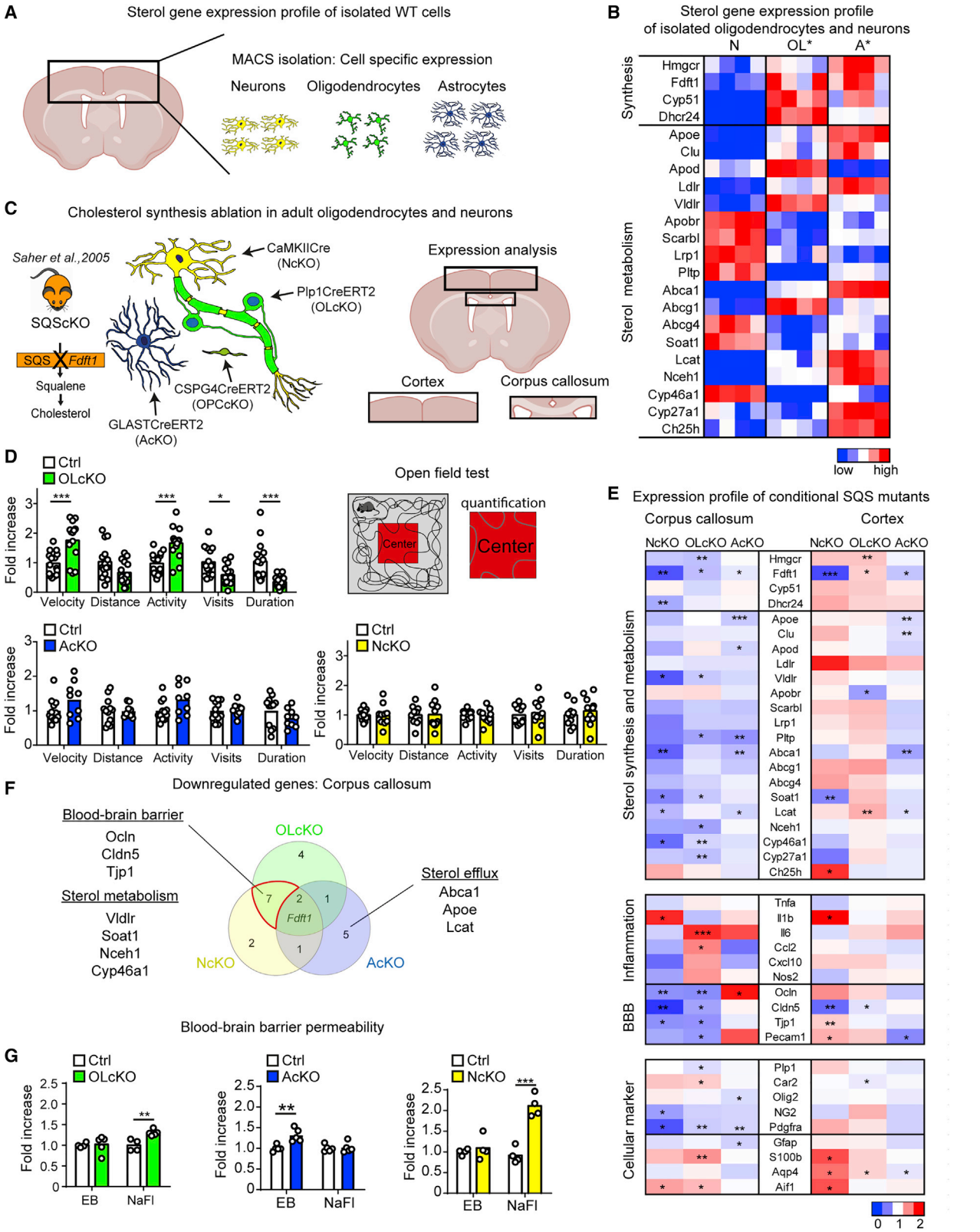

(legend on next page)

by providing cholesterol in apolipoprotein E (ApoE)-containing lipoproteins (Dietschy, 2009), and the lack of this support in the diseased CNS contributes to the disruption of CNS cholesterol homeostasis. However, neuronal responses to myelin degeneration with regard to cholesterol metabolism, as well as the role of neuronal cholesterol in remyelination, remain unknown.

Here, we show that during chronic myelin disease, neurons increase cholesterol synthesis. Similarly, neurons in MS brain upregulate a gene profile related to cholesterol synthesis and metabolism in non-lesion areas. Our data support the essential role of neuronal cholesterol for remyelination, a role that is likely relevant for MS disease progression.

RESULTS

Loss of *Fdft1* in neurons alters white matter cholesterol metabolism

In the adult brain, neuronal synthesis and horizontal transfer from glial cells meet neuronal cholesterol demands. To evaluate neuronal versus glial cholesterol metabolism, we acutely isolated neurons, astrocytes, and oligodendrocytes from cortex or subcortical white matter of adult mice (Figure 1A). The abundance of neuronal mRNA transcripts related to cholesterol metabolism was compared with oligodendrocyte and astrocyte profiles obtained previously (Berghoff et al., 2021). Compared with oligodendrocytes and astrocytes, neurons showed low steady-state expression levels of cholesterol synthesis genes (Figure 1B; Table S1). In contrast, several gene transcripts related to cholesterol import (*Apobr*, *Scarb1*, *Lrp1*), storage (*Soat1*), and brain export (*Cyp46a1*) were higher in relative abundance. To assess the relevance of cell-type-specific cholesterol synthesis, we genetically inactivated squalene synthase (SQS; *Fdft1* gene), an essential enzyme of the sterol biosynthesis pathway, in adult oligodendrocytes (OL, OLcKO), oligodendrocyte precursor cells (OPC, OPCcKO), astrocytes (AcKO), or neurons (NcKO) (Figures 1C, S1A, and S1B) (Berghoff et al., 2021; Fünfschilling et al., 2012; Saher et al., 2005). Comparable with oligodendroglial and astrocyte mutants (Berghoff et al., 2021), loss of cholesterol synthesis in neurons did not affect peripheral serum cholesterol level or body weight (Figure S1C). In an open-field test, only OLcKO animals showed signs of anxiety (Figures 1D, S1D, and S1E), which were enhanced in OPC/oligodendrocyte double mutants (Figure S1F). Notably, these behavioral changes occurred in the absence of overt myelin/oligodendrocyte deficits (Figure S1G).

Next, we evaluated the impact of conditional loss of SQS/cholesterol synthesis by gene transcription profiling of cortex or subcortical white matter (corpus callosum). In the cortex, conditional inactivation of cholesterol synthesis in neurons or oligodendrocytes resulted in moderate upregulation of cholesterol synthesis genes, possibly to compensate for the loss of cholesterol synthesis in the affected cell type (Figure 1E; Table S2). In contrast, in all conditional mutants, we observed a moderate but consistent downregulation of expression related to cholesterol metabolism in white matter (Figures 1E, 1F, and S1H). Here, reduced expression of genes associated with cholesterol transport was noted in all conditional mutants, particularly in AcKO animals (Figure 1F). In agreement, sterol profiling revealed only moderate alteration in conditional mutants (Figure S2A).

Surprisingly, corpus callosum of OLcKO and NcKO mice revealed a marked downregulation of genes related to the blood-brain barrier (BBB). This was accompanied by upregulation of a few inflammatory mediators with profiles being unique to each mutant (Figures 1E and 1F). Interestingly, by biochemical quantification of BBB permeability, the reduced tight junction gene expression was paralleled by increased CNS influx of the small-molecular-weight BBB tracer sodium fluorescein (NaFl; 376 Da) in OLcKO and NcKO brains. This was not the case in AcKO animals (Figures 1F, S1D, S2B, and S2C).

In summary, genetic elimination of cholesterol synthesis in oligodendrocytes, neurons, and astrocytes leads to altered expression of genes related to cholesterol metabolism in gray and white matter. These data confirm that all cell types contribute to cholesterol homeostasis in the adult brain by cell-autonomous cholesterol synthesis. Of note, in cortex but also corpus callosum of neuronal mutants, *Fdft1* expression was significantly reduced, and the abundance of cholesterol synthesis intermediates was attenuated (Figures 1E and S2A). This suggests axonal localization of cholesterol synthesis transcripts *in vivo*, contrary to cultured neurons (Vance et al., 2000).

Myelin disease leads to increased cholesterol synthesis in neurons

Even subtle myelin defects can lead to axonal damage, myelin instability, and glial activation, as observed in null mutants of the myelin-specific genes *Plp1* (proteolipid protein 1) and *Cnp1* (2′,3′-cyclic-nucleotide 3′-phosphodiesterase) (Edgar et al., 2004, 2009; Lappe-Siefke et al., 2003; Trevisiol et al., 2020). To assess neuronal responses to mild alterations in myelin integrity, we genetically labeled neuronal nuclei, predominantly of callosal projection neurons (CPNs) in *Plp1* and

Figure 1. Loss of cholesterol synthesis in oligodendrocytes, astrocytes, and neurons

(A) Scheme of magnetic cell separation (MACS) from the indicated brain region.

(B) Gene expression profile of isolated neurons (N), oligodendrocytes (OL), and astrocytes (A) from n = 4 wild-type animals (Berghoff et al., 2021).

(C) Scheme of isolation of boxed brain regions from oligodendrocyte (OLcKO), astrocyte (AcKO), and neuronal (NcKO) cholesterol synthesis-deficient (*Fdft1*$^{fl/fl}$) animals.

(D) Open-field test of OLcKO (n = 14), AcKO (n = 9), and NcKO (n = 8–11) animals compared with controls (n = 10–15) in the center (two-sided Student's t test).

(E) Expression profile of genes related to cholesterol metabolism, inflammation, BBB, and cell markers in tissues of conditional mutants. Heatmaps show mean fold expression of biological replicates (n = 4–7) normalized to controls (two-sided Student's t test).

(F) Venn diagram of downregulated genes in corpus callosum of animals in (E).

(G) Extravasated Evans blue (EB) and sodium fluorescein (NaFl) in oligodendrocyte (OLcKO, n = 5), astrocyte (AcKO, n = 5), and neuronal (NcKO, n = 4) mutants compared with controls (n = 4; two-sided Student's t test).

***p < 0.001, **p < 0.01, *p < 0.05.

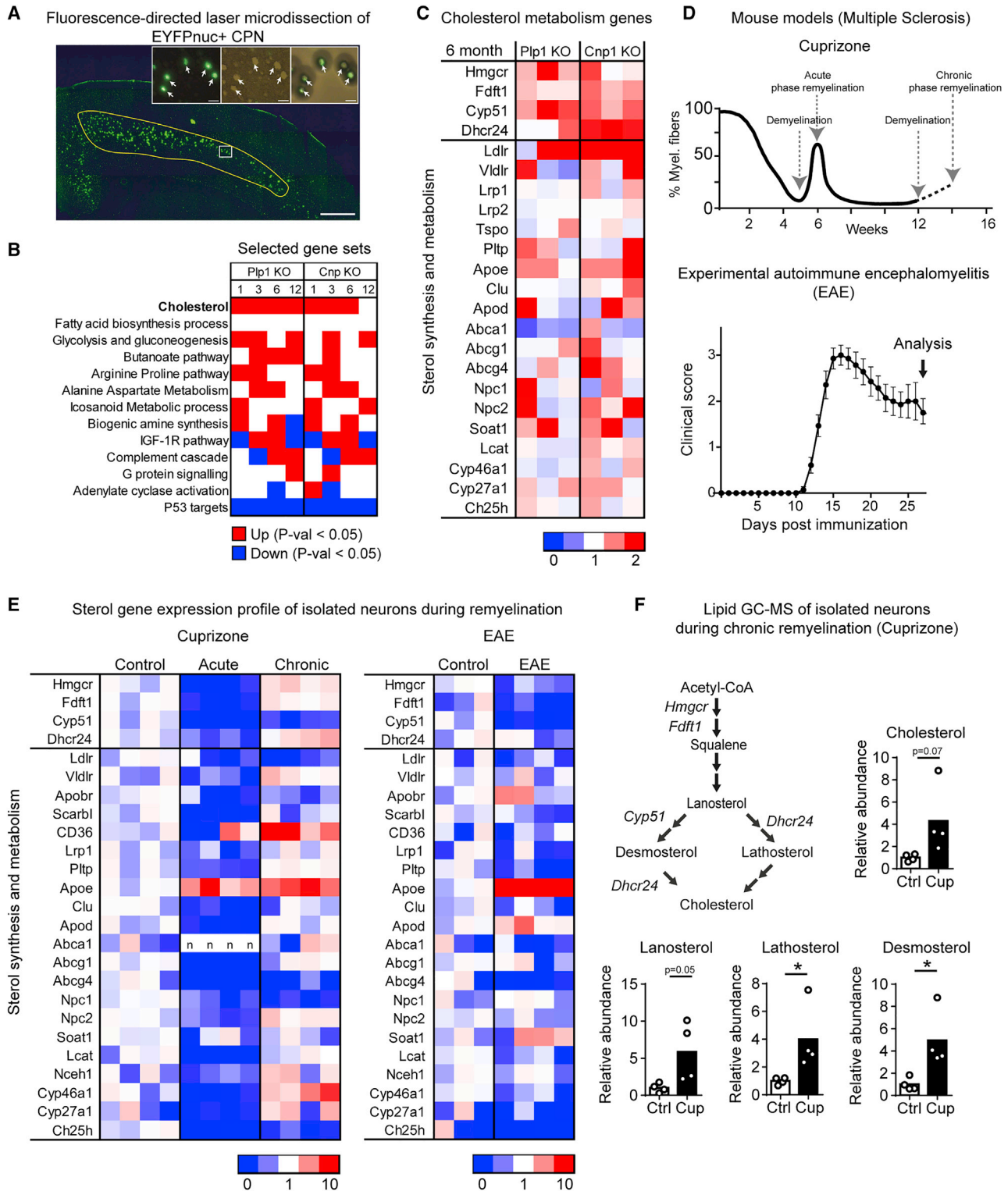

Figure 2. Expression of genes related to cholesterol metabolism in neurons of genetic and experimental myelin disease models

(A) Fluorescence-directed laser microdissection of EYFPnuc^{+} CPNs from the primary motor and somatosensory cortex (yellow line) of PLP-KO and CNP-KO mutants (scale bar: 200 μm). Insets show the tissue section before and after laser microdissection and isolated neurons (scale bars: 20 μm).

(B) Selected gene sets in microdissected neurons from PLP-KO and CNP-KO mutants compared with controls (1, 3, 6, and 12 months of age, n = 3 animals per group). Significantly altered gene sets (GSEA, $p < 0.05$) are indicated in red and blue.

(legend continued on next page)

Cnp1 knockout mice, with the Thy1-EYFPnuc transgene (Wehr et al., 2006). Despite the axonal pathology, CPN loss was not a feature of *Plp1* and *Cnp1* mutants as quantified by EYFPnuc$^+$ cell counting (Figure S2D). We then isolated CPNs from cortical layer five by fluorescence-directed laser microdissection from 1 to 12 months of age for transcriptional profiling (Figures 2A and S2E). Transcriptional profiling revealed 412 differentially expressed genes in CPN from *Cnp1* knockout mice and 104 genes from *Plp1* knockout mice compared with Thy1-EYFPnuc controls (adjusted [adj.] $p < 0.001$, Benjamin-Hochberg correction > 1.8-fold changes) (Figure S2F). Surprisingly, by gene set enrichment analysis (GSEA), the gene set "cholesterol metabolism" was upregulated in CPNs of both mutants (Figure 2B). This included genes involved in cholesterol synthesis (*Hmgcr*, *Fdft1*, *Cyp51*, *Dhcr24*) and transport (*Ldlr*, *Apoe*) (Figure 2C; Table S2).

Because neuronal upregulation of genes related to cholesterol metabolism could be a general response to chronic myelin alterations, we analyzed transcriptional profiles of isolated cortical neurons following acute experimental autoimmune encephalomyelitis (EAE) induction and following acute-phase (6 weeks of cuprizone) and chronic-phase remyelination (12 weeks of cuprizone followed by 2 weeks of cuprizone withdrawal, 12+2 weeks) (Figure 2D). During acute disease (EAE or 6 weeks of cuprizone), neurons consistently downregulated gene expression related to cholesterol metabolism (Figure 2E). In contrast, during remyelination following chronic demyelination in the cuprizone model, expression of genes involved in cholesterol metabolism was increased (Figure 2E; Table S3). To test whether the upregulation of cholesterol synthesis genes was functionally relevant, we determined the abundance of sterols by gas chromatography coupled to mass spectrometry (GC/MS) in the chronic remyelination paradigm. Cholesterol and several precursors of the cholesterol synthesis pathway were increased 4- to 5-fold in isolated neurons (Figure 2F), suggesting enhanced cholesterol synthesis in neurons during remyelination in this paradigm.

Increased cholesterol synthesis gene expression in neurons from patients with MS

We next determined whether increased neuronal expression of cholesterol synthesis genes is relevant in human MS and used single-nuclei gene expression profiles (snRNAseq) from patients with MS and healthy control tissue from two recent studies (GEO: GSE118257 and GSE124335). We separately merged expression profiles of neurons, oligodendrocytes, and astrocytes as annotated in each study (Figures 3A, 3B, and S3A–S3C). Although the disease history of the MS tissue samples is unknown, we categorized MS samples in the subsets "lesion" (comprising active MS lesions) and "non-lesion" (containing normal-appearing MS tissue). Neuronal nuclei contributed to each of the MS subsets (3,122 lesion, 3,547 non-lesion). Next, we performed pairwise comparisons of expression profiles separately, in neurons, oligodendrocytes, or astrocytes, focusing on cholesterol metabolism.

Lesion-derived astrocytes showed significantly reduced transcript levels of several genes related to cholesterol synthesis (*HMGCR*, *FDFT1*, *DHCR7*, *DHCR24*), while this gene set was not differentially regulated in non-lesion-derived astrocytes (Figure 3C). In contrast, both oligodendrocytes and neurons in MS lesions increased expression of apolipoproteins, including *APOE*, indicating participation in lipid transport in areas of active disease. Moreover, MS oligodendrocytes upregulated genes associated with cholesterol synthesis and metabolism, most markedly in lesions. This confirms the relevance of oligodendroglial cholesterol in myelin disease (Berghoff et al., 2017b, 2021; Voskuhl et al., 2019) and potentially reflects ongoing remyelination or attempts to remyelinate. Notably, neurons in MS lesions showed reduced levels of genes associated with cholesterol synthesis, including the rate-limiting enzyme of this process, *HMGCR* (Figure 3C). In contrast, in non-lesion MS tissue, neurons upregulated this gene set, suggesting increased neuronal cholesterol synthesis in normal-appearing MS tissue areas.

Neuronal *Fdft1* ablation impairs remyelination following chronic cuprizone

The contrasting expression of neuronal cholesterol synthesis genes in lesion versus non-lesion areas of MS brain and in remyelination after acute versus chronic demyelination in mouse models prompted us to test the importance of this finding for lesion repair. We determined efficiency of repair in neuronal SQS mutants (NcKO) challenged with acute and chronic demyelination paradigms and evaluated disease expression, remyelination (Gallyas), oligodendrocyte differentiation (CAII), number of oligodendrocyte linage cells (Olig2), and gliosis (GFAP, Iba1, MAC3).

Loss of neuronal cholesterol synthesis did not affect acute-phase remyelination in cuprizone-treated mice (Figures 4A, 4B, and S4A–S4C; Video S1) or pathology following immune-mediated myelin degeneration (Figures 4C–4E). However, after cuprizone-induced chronic demyelination, we observed reduced oligodendrocyte density and impaired remyelination in both the corpus callosum and the cortex of NcKO animals (Figures 4F–4H and S4A–S4C). This defective repair occurred without affecting gliosis, neuronal degeneration (NeuN$^+$ cell number, Fluoro-Jade, TUNEL) or axonal stress (APP$^+$ spheroids) (Figure S4D–S4F). The degree of sustained hypomyelination in NcKO animals was comparable with mutants with inactivated *Fdft1* in OPCs (NcKO: 53% ± 5% of controls; OPCcKO: 55% ± 3%; Figure 4I). Both conditional mutants displayed comparable defects in motor performance after chronic cuprizone

(C) Fold expression of genes related to cholesterol metabolism in CPNs from PLP-KO and CNP-KO mutants at 6 months of age (n = 3) normalized to controls.
(D) Time points of analysis in the cuprizone model and EAE animals analyzed in (E).
(E) Profile of gene expression related to cholesterol metabolism in isolated neurons following acute (6 weeks) and chronic (12w+2w) cuprizone (left) and in EAE (right) showing fold expression normalized to controls (n = 3–4 animals).
(F) Cholesterol synthesis pathway with major enzymes and sterol intermediates. Mean relative abundance of sterols in isolated neurons from chronic cuprizone-treated mice compared with controls (n = 4), measured by GC-MS (two-sided Student's t test).

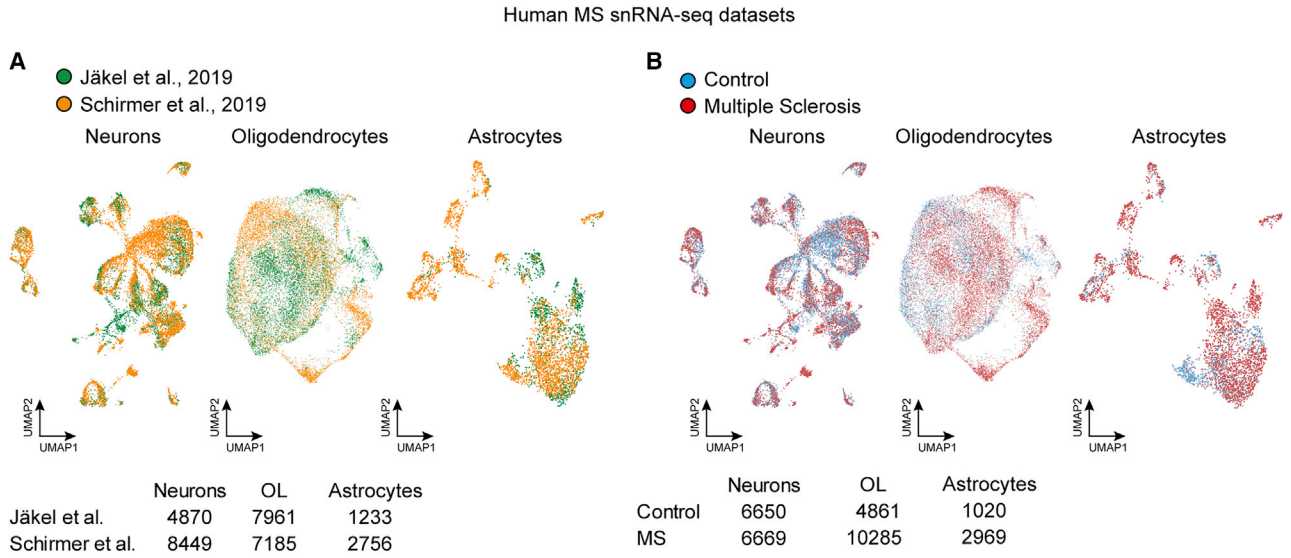

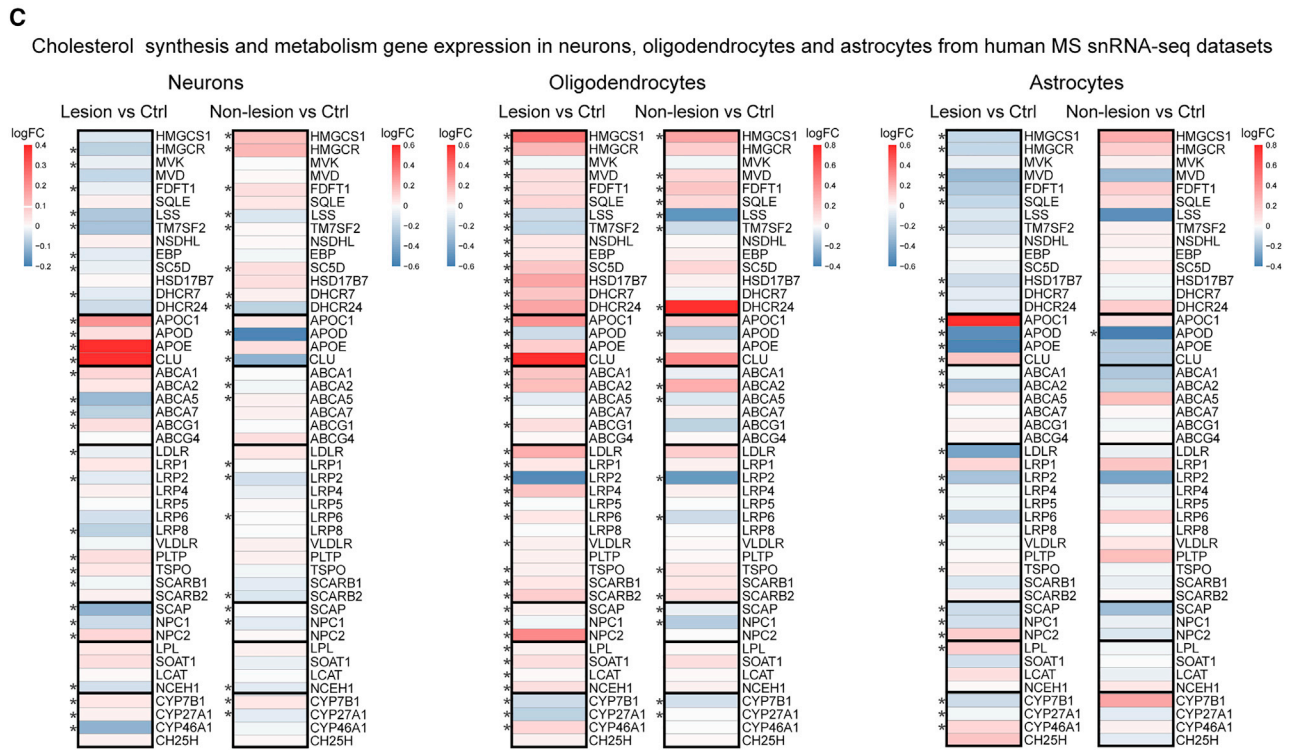

Figure 3. Gene expression related to cholesterol metabolism in neurons, oligodendrocytes, and astrocytes from patients with MS

(A) UMAP (uniform manifold approximation and projection) of neurons, oligodendrocytes, and astrocytes from two merged human MS snRNA-seq datasets (GEO: GSE118257 and GSE124335).

(B) UMAPs as in (A) depicting patient samples identity.

(C) Heatmap of mean $\log_2$ fold changes (logFC) of gene expression related to cholesterol metabolism comparing control and MS (lesion and non-lesion) samples (Wilcoxon rank-sum test, two-sided).

administration (Figure S4G). However, in contrast with OPC mutants, the loss of neuronal cholesterol synthesis caused a reduction of Olig2/PCNA$^+$ proliferating OPCs in the corpus callosum (Figures 4G, 4I, and 4J). Interestingly, cholesterol administration enhanced OPC proliferation and differentiation in myelinating co-cultures, which was largely abolished by eliminating neuronal activity (Figures 4K and S4H). Together, these findings raise the possibility that elevating neuronal cholesterol synthesis is essential for OPC proliferation and differentiation to facilitate remyelination.

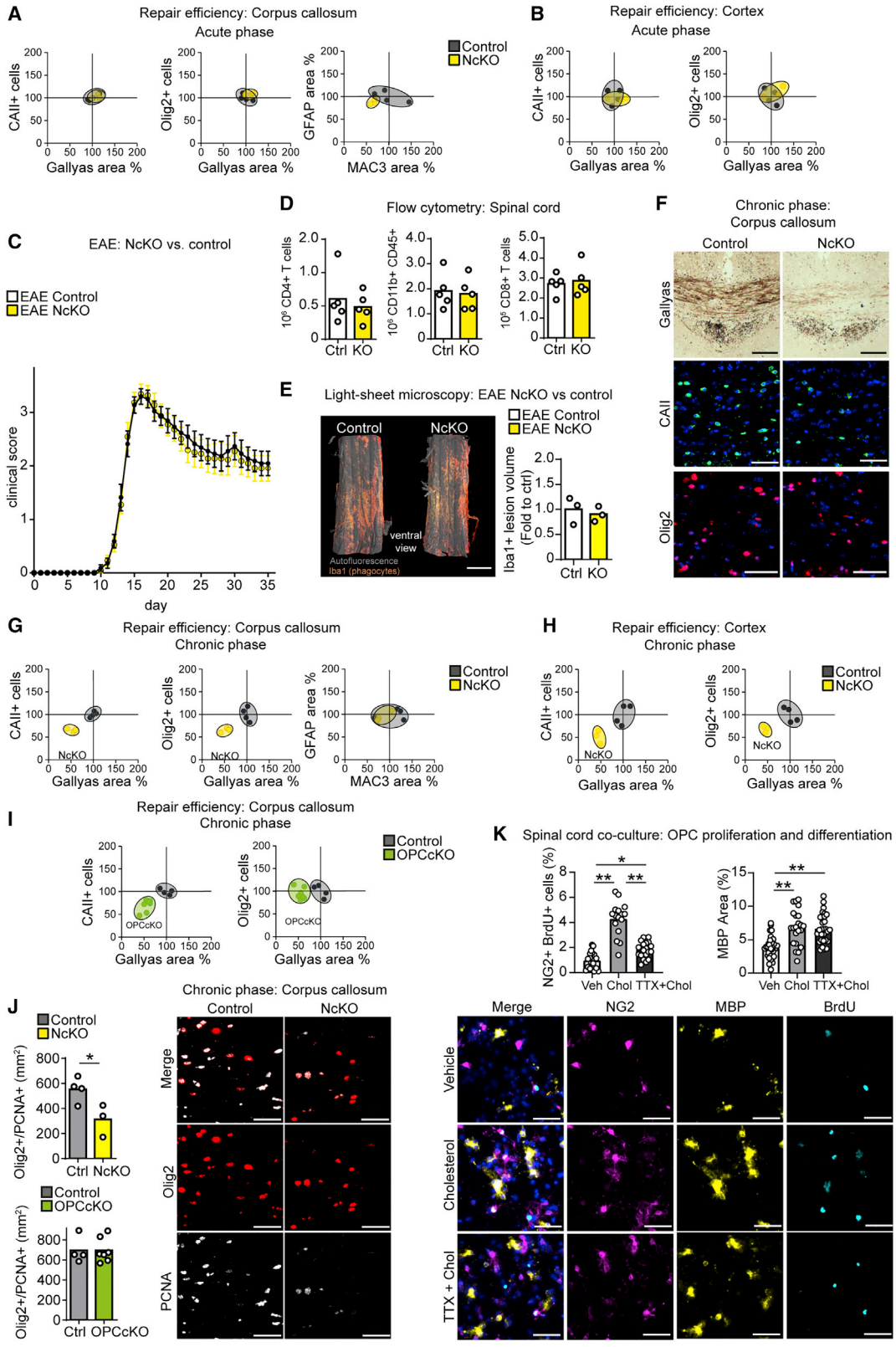

(legend on next page)

DISCUSSION

Complete functional recovery from demyelinating episodes and prevention of persistent disabilities is the ultimate goal of MS therapies. In addition to decreasing the rate of demyelinating events and dampening pathological inflammation, the support of remyelination has come into focus in MS drug development. Repair following degeneration of oligodendrocytes and destruction of myelin involves the resolution of inflammation, OPC migration, proliferation, and differentiation (Reich et al., 2018). Tissue regeneration is achieved by synthesis of lipid- and cholesterol-rich myelin membranes by newly differentiated oligodendrocytes and oligodendrocytes that survived the immune attack (Franklin et al., 2021). Remyelination contributes to neuroprotection and the restoration of impulse conduction and may facilitate (re)establishing neural circuits (Bacmeister et al., 2020).

Disparate repair processes during acute and chronic myelin disease

With respect to lipid metabolism, repair after an acute demyelinating episode differs markedly from repair in chronic myelin disease or after repeated demyelinating events. Tissue remodeling and repair after an acute demyelinating attack is coordinated by microglial/macrophage activation and lipid recycling (Berghoff et al., 2021; Cunha et al., 2020; Miron et al., 2013). Correspondingly, acute-phase remyelination is independent of *Fdft1* inactivation in oligodendrocytes, OPCs, astrocytes, or neurons (this study and Berghoff et al., 2021).

In chronic myelin disease, myelin debris is largely cleared from demyelinated lesions. In chronically demyelinated lesions in cuprizone-treated mice (Berghoff et al., 2017b) and in chronically inactive lesions in patients with MS (Heβ et al., 2020), the remaining microglia/macrophages appear lipid laden and foamy, suggesting that lipid recycling could be inefficient. These lipid trafficking defects in microglia could not only impede remyelination but also aggravate axonal damage, as observed in TREM2 mutants (Cantoni et al., 2015).

Because cholesterol is essential for myelin formation (Saher et al., 2005), these findings underscore the necessity of local *de novo* synthesis. This is supported by the observation that statin-mediated inhibition of cholesterol synthesis blocks remyelination (Miron et al., 2009). However, astrocytes, which provide cholesterol in the healthy brain, fail as a local cholesterol source in myelin disease both in mouse models (Berghoff et al., 2021; Borggrewe et al., 2021; Itoh et al., 2018) and in MS lesions (this study). We hypothesize that chronic myelin disease depletes local cholesterol levels, which triggers cell-autonomous cholesterol synthesis by feedback regulation. In agreement, the cholesterol for remyelination originates at least partially from *de novo* oligodendroglial synthesis (Berghoff et al., 2021; Jurevics et al., 2002; Voskuhl et al., 2019). The finding that dietary cholesterol supplementation also supports myelin repair (Berghoff et al., 2017b; Saher et al., 2012) suggests that endogenous cholesterol synthesis is insufficient for complete remyelination. In the current study, we provide evidence that neuronal cholesterol synthesis is essential for repair of chronically demyelinated lesions.

Neuronal cholesterol synthesis during remyelination

Following chronic demyelination, we found impaired remyelination in animals lacking neuronal cholesterol synthesis. In agreement, neuronal expression of cholesterol synthesis genes is increased in human non-lesion MS tissue and following chronic experimental demyelination. In neuronal mutants of cholesterol synthesis, but not in corresponding oligodendroglial mutants, we showed a marked reduction in the density of oligodendrocyte lineage cells. This finding points to an inference with repair that precedes myelin membrane synthesis, likely in OPC proliferation and oligodendrocyte differentiation.

What is the mechanism by which regeneration of chronically demyelinated white matter tracts benefits from neuronal cholesterol synthesis? Neuronal electrical activity triggers OPC proliferation and oligodendrocyte differentiation after demyelination through unknown signals (Marisca et al., 2020; Mitew et al., 2018; Ortiz et al., 2019). The hyperactivity of cortical neurons observed after acute demyelination (Bacmeister et al., 2020) could offset conduction deficits of demyelinated white matter tracts (Crawford et al., 2009). This could lead to cholesterol-rich synaptic vesicle release from callosal axons (Almeida et al., 2020; Pfeiffer et al., 2019) and provide the signal to OPCs to proliferate. We show that administration of cholesterol

Figure 4. Neuronal *Fdft1* ablation impairs remyelination following chronic cuprizone

(A and B) Repair efficiency in the corpus callosum (A) and cortex (B) during acute 6-week cuprizone in NcKO (n = 3 animals) compared with controls (n = 4, set to 100%) based on histochemical stainings for myelin (Gallyas), oligodendrocytes (CAII), oligodendrocyte lineage cells (Olig2), microgliosis (MAC3), and astrogliosis (GFAP), shown as 95% confidence ellipses with individual data points.

(C) Mean clinical EAE score ± SEM of control and NcKO mice (n = 11).

(D) Flow cytometric quantification of inflammatory cells of EAE animals in (C) (n = 5).

(E) Light sheet microcopy of lumbar spinal cord from NcKO and controls 35 days after EAE induction, stained for Iba1$^+$ phagocytes (n = 3).

(F) Representative micrographs of the corpus callosum of control and NcKO animals following chronic cuprizone (12w+2w) illustrating myelination (Gallyas), oligodendrocytes (CAII), and oligodendrocyte lineage cells (Olig2).

(G and H) Repair efficiency in the corpus callosum (G) and cortex (H) during chronic cuprizone (12w+2w) in NcKO mice (n = 4) compared with controls (n = 3, set to 100%).

(I) Repair efficiency in the corpus callosum during chronic 12w+2w cuprizone in OPC cholesterol mutants (OPCcKO, n = 7) compared with controls (n = 4, set to 100%).

(J) Representative micrographs of Olig2/PCNA double labeling in the corpus callosum with quantification of NcKO (n = 3) and OPCcKO (n = 7) mutants compared with controls (n = 4) following chronic remyelination (12w+2w; two-sided Student's t test).

(K) Mean density of proliferating OPCs (NG2$^+$, BrdU$^+$ cells normalized to DAPI$^+$ cells) and mean oligodendrocyte differentiation (MBP$^+$ area) in spinal cord cultures at 17 days *in vitro* (16–31 images from n = 2–3 cultures) in the presence of cholesterol (10 μg/mL) with or without inhibition of neuronal activity by tetrodotoxin (TTX; 1 μM) with individual values (one-way ANOVA with Sidak's post-test).

**p < 0.01, *p < 0.05. Scale bars: 50 μm (F, J, K), 1 mm (E).

facilitates OPC proliferation. However, OPC proliferation was amplified only when cholesterol was supplied in the context of neuronal activity. It is possible that neurotransmitter release occurs concomitant with release of neuronal cholesterol to prevent (premature) OPC differentiation and to generate sufficient numbers of oligodendrocyte lineage cells to accomplish repair.

In addition, cholesterol-depleted denuded axons as in chronic lesions of NcKO mice are likely more fragile as suggested from membrane tether forces of cholesterol synthesis mutant neurons (Fünfschilling et al., 2012). Especially when electrically hyperactive, impaired stability of axonal membranes could increase axon damage and the probability of conduction blocks.

Dietary cholesterol supplementation during chronic-phase remyelination increases the density of proliferating OPCs (Berghoff et al., 2017b), suggesting that the entire oligodendrocyte lineage can benefit from externally administered cholesterol. It is possible that neurons increase cholesterol production also to support oligodendroglia. Indeed, cholesterol released from callosal axons would position the lipid optimally to supply proliferating OPCs and newly differentiating oligodendrocytes. This suggestion is reinforced by the observation that electrically hyperactive neurons in demyelinated lesions release lipids as ApoE-containing lipoproteins (Ioannou et al., 2019; Xu et al., 2006). Our data show that increased neuronal cholesterol synthesis is paralleled by strongly elevated expression of ApoE. Thus, following chronic demyelination, neurons could export cholesterol via ApoE to support myelination by oligodendrocytes in a lipid-poor environment. Although we have not measured neuronal activity in demyelinated conditional mutants, we speculate that *Fdft1* mutant neurons produce less activity-dependent pro-repair signals to local OPCs than controls.

Taken together, our data show that loss of neuronal cholesterol synthesis strongly impairs remyelination with relevance for human MS disease. Our study confirms distinct cell-type-specific roles in brain cholesterol biogenesis and import during remyelination and provides an additional explanation for disease progression related to age-associated decline of cholesterol synthesis (Berghoff et al., 2021; Scalfari, 2019; Thelen et al., 2006). Further studies are needed to design therapeutic strategies that stimulate cholesterol synthesis in affected neuronal populations.

STAR★METHODS

Detailed methods are provided in the online version of this paper and include the following:

- KEY RESOURCES TABLE
- RESOURCE AVAILABILITY
  - Lead contact
  - Materials availability
  - Data and code availability
- EXPERIMENTAL MODEL AND SUBJECT DETAILS
- METHOD DETAILS
  - Tamoxifen induced recombination
  - Experimental autoimmune encephalomyelitis (EAE)
  - Cuprizone
  - Serum Analysis
  - Open field
  - Blood-brain barrier permeability
  - Flow cytometry
  - Magnetic cell isolation (MACS)
  - Expression analyses
  - Histochemistry
  - Quantification of sterols
  - Light sheet microscopy
  - Laser capture microdissection
  - Microarray expression analysis
  - Human single-nuclei transcriptome sequencing datasets
  - Spinal cord co-cultures
  - Whole cell current clamp and microelectrode arrays
- QUANTIFICATION AND STATISTICAL ANALYSIS

SUPPLEMENTAL INFORMATION

Supplemental information can be found online at https://doi.org/10.1016/j.celrep.2021.109889.

ACKNOWLEDGMENTS

We cordially thank Annette Fahrenholz, Annika M. Schmidke, and Tanja Freerck for technical support and Dr. Matthew Euston for supplying myelinating cell cultures. We thank Charles Stiles, John Alberta, and Said Ghandour for generous gifts of antibodies. This work was funded by the Deutsche Forschungsgemeinschaft (SA 2014/2-1 to G.S.), the Wilhelm Sander-Stiftung (grant 2019.138.1 to G.S.), the Alzheimer Forschung Initiative (grant 19070 to G.S.), the UK MS Society (grant 127 to J.M.E.), the Adelson Medical Research Foundation (to K.A.N.), and Medical Research Scotland (PhD studentship 791-2014 to E.R.B.).

AUTHOR CONTRIBUTIONS

S.A.B. and G.S. planned and designed the study. S.A.B. and L.S. were involved in all experiments. T.S., Y.Z., and S.B. performed reanalysis of human snRNA-seq datasets. L.H. and F.O. did flow cytometry. T.I. and P.S. performed lipid mass spectrometry. M.H.V. performed histology. C.D. and A.O.S. did light sheet microscopy. D.K.-B. was involved in behavior experiments. S.W., K.-A.N., and M.R. analyzed genetic myelin mutants. J.M.E. conducted myelinating cell culture experiments. K.M. and E.R.B. conducted electrophysiology experiments on myelinating cell cultures. S.A.B. and G.S. wrote and edited the manuscript. All authors approved the manuscript.

DECLARATION OF INTERESTS

The authors declare no competing interests.

Received: March 30, 2021
Revised: August 12, 2021
Accepted: October 5, 2021
Published: October 26, 2021

REFERENCES

Almeida, R.G., Williamson, J.M., Madden, M.E., Early, J.J., Voas, M.G., Talbot, W.S., Bianco, I.H., and Lyons, D.A. (2020). Synaptic vesicle fusion along axons is driven by myelination and subsequently accelerates sheath growth in an activity-regulated manner. bioRxiv. https://doi.org/10.1101/2020.08.28.271593.

Bacmeister, C.M., Barr, H.J., McClain, C.R., Thornton, M.A., Nettles, D., Welle, C.G., and Hughes, E.G. (2020). Motor learning promotes remyelination via new and surviving oligodendrocytes. Nat. Neurosci. *23*, 819–831.

Berghoff, S.A., Düking, T., Spieth, L., Winchenbach, J., Stumpf, S.K., Gerndt, N., Kusch, K., Ruhwedel, T., Möbius, W., and Saher, G. (2017a). Blood-brain

barrier hyperpermeability precedes demyelination in the cuprizone model. Acta Neuropathol. Commun. *5*, 94.

Berghoff, S.A., Gerndt, N., Winchenbach, J., Stumpf, S.K., Hosang, L., Odoardi, F., Ruhwedel, T., Böhler, C., Barrette, B., Stassart, R., et al. (2017b). Dietary cholesterol promotes repair of demyelinated lesions in the adult brain. Nat. Commun. *8*, 14241.

Berghoff, S.A., Spieth, L., Sun, T., Hosang, L., Schlaphoff, L., Depp, C., Düking, T., Winchenbach, J., Neuber, J., Ewers, D., et al. (2021). Microglia facilitate repair of demyelinated lesions via post-squalene sterol synthesis. Nat. Neurosci. *24*, 47–60.

Bijland, S., Thomson, G., Euston, M., Michail, K., Thümmler, K., Mücklisch, S., Crawford, C.L., Barnett, S.C., McLaughlin, M., Anderson, T.J., et al. (2019). An in vitro model for studying CNS white matter: functional properties and experimental approaches. F1000Res. *8*, 117.

Borggrewe, M., Grit, C., Vainchtein, I.D., Brouwer, N., Wesseling, E.M., Laman, J.D., Eggen, B.J.L., Kooistra, S.M., and Boddeke, E.W.G.M. (2021). Regionally diverse astrocyte subtypes and their heterogeneous response to EAE. Glia *69*, 1140–1154.

Butler, A., Hoffman, P., Smibert, P., Papalexi, E., and Satija, R. (2018). Integrating single-cell transcriptomic data across different conditions, technologies, and species. Nat. Biotechnol. *36*, 411–420.

Camargo, N., Brouwers, J.F., Loos, M., Gutmann, D.H., Smit, A.B., and Verheijen, M.H. (2012). High-fat diet ameliorates neurological deficits caused by defective astrocyte lipid metabolism. FASEB J. *26*, 4302–4315.

Cantoni, C., Bollman, B., Licastro, D., Xie, M., Mikesell, R., Schmidt, R., Yuede, C.M., Galimberti, D., Olivecrona, G., Klein, R.S., et al. (2015). TREM2 regulates microglial cell activation in response to demyelination in vivo. Acta Neuropathol. *129*, 429–447.

Crawford, D.K., Mangiardi, M., Xia, X., López-Valdés, H.E., and Tiwari-Woodruff, S.K. (2009). Functional recovery of callosal axons following demyelination: a critical window. Neuroscience *164*, 1407–1421.

Cunha, M.I., Su, M., Cantuti-Castelvetri, L., Müller, S.A., Schifferer, M., Djannatian, M., Alexopoulos, I., van der Meer, F., Winkler, A., van Ham, T.J., et al. (2020). Pro-inflammatory activation following demyelination is required for myelin clearance and oligodendrogenesis. J. Exp. Med. *217*, e20191390.

Dietschy, J.M. (2009). Central nervous system: cholesterol turnover, brain development and neurodegeneration. Biol. Chem. *390*, 287–293.

Dietschy, J.M., and Turley, S.D. (2004). Thematic review series: brain Lipids. Cholesterol metabolism in the central nervous system during early development and in the mature animal. J. Lipid Res. *45*, 1375–1397.

Edgar, J.M., McLaughlin, M., Yool, D., Zhang, S.C., Fowler, J.H., Montague, P., Barrie, J.A., McCulloch, M.C., Duncan, I.D., Garbern, J., et al. (2004). Oligodendroglial modulation of fast axonal transport in a mouse model of hereditary spastic paraplegia. J. Cell Biol. *166*, 121–131.

Edgar, J.M., McLaughlin, M., Werner, H.B., McCulloch, M.C., Barrie, J.A., Brown, A., Faichney, A.B., Snaidero, N., Nave, K.A., and Griffiths, I.R. (2009). Early ultrastructural defects of axons and axon-glia junctions in mice lacking expression of Cnp1. Glia *57*, 1815–1824.

Franklin, R.J.M., Frisén, J., and Lyons, D.A. (2021). Revisiting remyelination: Towards a consensus on the regeneration of CNS myelin. Semin. Cell Dev. Biol. *116*, 3–9.

Fünfschilling, U., Jockusch, W.J., Sivakumar, N., Möbius, W., Corthals, K., Li, S., Quintes, S., Kim, Y., Schaap, I.A., Rhee, J.S., et al. (2012). Critical time window of neuronal cholesterol synthesis during neurite outgrowth. J. Neurosci. *32*, 7632–7645.

Heberle, H., Meirelles, G.V., da Silva, F.R., Telles, G.P., and Minghim, R. (2015). InteractiVenn: a web-based tool for the analysis of sets through Venn diagrams. BMC Bioinformatics *16*, 169.

Heß, K., Starost, L., Kieran, N.W., Thomas, C., Vincenten, M.C.J., Antel, J., Martino, G., Huitinga, I., Healy, L., and Kuhlmann, T. (2020). Lesion stage-dependent causes for impaired remyelination in MS. Acta Neuropathol. *140*, 359–375.

Huang, W., Zhao, N., Bai, X., Karram, K., Trotter, J., Goebbels, S., Scheller, A., and Kirchhoff, F. (2014). Novel NG2-CreERT2 knock-in mice demonstrate heterogeneous differentiation potential of NG2 glia during development. Glia *62*, 896–913.

Ioannou, M.S., Jackson, J., Sheu, S.H., Chang, C.L., Weigel, A.V., Liu, H., Pasolli, H.A., Xu, C.S., Pang, S., Matthies, D., et al. (2019). Neuron-Astrocyte Metabolic Coupling Protects against Activity-Induced Fatty Acid Toxicity. Cell *177*, 1522–1535.e14.

Itoh, N., Itoh, Y., Tassoni, A., Ren, E., Kaito, M., Ohno, A., Ao, Y., Farkhondeh, V., Johnsonbaugh, H., Burda, J., et al. (2018). Cell-specific and region-specific transcriptomics in the multiple sclerosis model: Focus on astrocytes. Proc. Natl. Acad. Sci. USA *115*, E302–E309.

Jäkel, S., Agirre, E., Mendanha Falcão, A., van Bruggen, D., Lee, K.W., Knuesel, I., Malhotra, D., Ffrench-Constant, C., Williams, A., and Castelo-Branco, G. (2019). Altered human oligodendrocyte heterogeneity in multiple sclerosis. Nature *566*, 543–547.

Jurevics, H., Largent, C., Hostettler, J., Sammond, D.W., Matsushima, G.K., Kleindienst, A., Toews, A.D., and Morell, P. (2002). Alterations in metabolism and gene expression in brain regions during cuprizone-induced demyelination and remyelination. J. Neurochem. *82*, 126–136.

Klugmann, M., Schwab, M.H., Jung, M., Puhlhofer, A., Schneider, A., Zimmermann, F., Griffiths, I.R., and Nave, K.A. (1997). Mutations of the proteolipid protein gene - A molecular mechanism of CNS dysmyelination. Altschul Sy *4*, 61–68.

Lappe-Siefke, C., Goebbels, S., Gravel, M., Nicksch, E., Lee, J., Braun, P.E., Griffiths, I.R., and Nave, K.A. (2003). Disruption of Cnp1 uncouples oligodendroglial functions in axonal support and myelination. Nat. Genet. *33*, 366–374.

Leone, D.P., Genoud, S., Atanasoski, S., Grausenburger, R., Berger, P., Metzger, D., Macklin, W.B., Chambon, P., and Suter, U. (2003). Tamoxifen-inducible glia-specific Cre mice for somatic mutagenesis in oligodendrocytes and Schwann cells. Mol. Cell Neurosci. *22*, 430–440.

Marisca, R., Hoche, T., Agirre, E., Hoodless, L.J., Barkey, W., Auer, F., Castelo-Branco, G., and Czopka, T. (2020). Functionally distinct subgroups of oligodendrocyte precursor cells integrate neural activity and execute myelin formation. Nat. Neurosci. *23*, 363–374.

Minichiello, L., Korte, M., Wolfer, D., Kühn, R., Unsicker, K., Cestari, V., Rossi-Arnaud, C., Lipp, H.P., Bonhoeffer, T., and Klein, R. (1999). Essential role for TrkB receptors in hippocampus-mediated learning. Neuron *24*, 401–414.

Miron, V.E., Zehntner, S.P., Kuhlmann, T., Ludwin, S.K., Owens, T., Kennedy, T.E., Bedell, B.J., and Antel, J.P. (2009). Statin therapy inhibits remyelination in the central nervous system. Am. J. Pathol. *174*, 1880–1890.

Miron, V.E., Boyd, A., Zhao, J.W., Yuen, T.J., Ruckh, J.M., Shadrach, J.L., van Wijngaarden, P., Wagers, A.J., Williams, A., Franklin, R.J.M., and Ffrench-Constant, C. (2013). M2 microglia and macrophages drive oligodendrocyte differentiation during CNS remyelination. Nat. Neurosci. *16*, 1211–1218.

Mitew, S., Gobius, I., Fenlon, L.R., McDougall, S.J., Hawkes, D., Xing, Y.L., Bujalka, H., Gundlach, A.L., Richards, L.J., Kilpatrick, T.J., et al. (2018). Pharmacogenetic stimulation of neuronal activity increases myelination in an axon-specific manner. Nat. Commun. *9*, 306.

Mori, T., Tanaka, K., Buffo, A., Wurst, W., Kühn, R., and Götz, M. (2006). Inducible gene deletion in astroglia and radial glia–a valuable tool for functional and lineage analysis. Glia *54*, 21–34.

Ortiz, F.C., Habermacher, C., Graciarena, M., Houry, P.Y., Nishiyama, A., Nait Oumesmar, B., and Angulo, M.C. (2019). Neuronal activity in vivo enhances functional myelin repair. JCI Insight *5*, 123434.

Otasek, D., Morris, J.H., Bouças, J., Pico, A.R., and Demchak, B. (2019). Cytoscape Automation: empowering workflow-based network analysis. Genome Biol. *20*, 185.

Pfeiffer, F., Frommer-Kaestle, G., and Fallier-Becker, P. (2019). Structural adaption of axons during de- and remyelination in the Cuprizone mouse model. Brain Pathol. *29*, 675–692.

Reich, D.S., Lucchinetti, C.F., and Calabresi, P.A. (2018). Multiple Sclerosis. N. Engl. J. Med. *378*, 169–180.

Rossner, M.J., Hirrlinger, J., Wichert, S.P., Boehm, C., Newrzella, D., Hiemisch, H., Eisenhardt, G., Stuenkel, C., von Ahsen, O., and Nave, K.A. (2006). Global transcriptome analysis of genetically identified neurons in the adult cortex. J. Neurosci. *26*, 9956–9966.

Saher, G., Brügger, B., Lappe-Siefke, C., Möbius, W., Tozawa, R., Wehr, M.C., Wieland, F., Ishibashi, S., and Nave, K.A. (2005). High cholesterol level is essential for myelin membrane growth. Nat. Neurosci. *8*, 468–475.

Saher, G., Rudolphi, F., Corthals, K., Ruhwedel, T., Schmidt, K.F., Löwel, S., Dibaj, P., Barrette, B., Möbius, W., and Nave, K.A. (2012). Therapy of Pelizaeus-Merzbacher disease in mice by feeding a cholesterol-enriched diet. Nat. Med. *18*, 1130–1135.

Scalfari, A. (2019). MS progression is predominantly driven by age-related mechanisms - YES. Mult. Scler. *25*, 902–904.

Schindelin, J., Arganda-Carreras, I., Frise, E., Kaynig, V., Longair, M., Pietzsch, T., Preibisch, S., Rueden, C., Saalfeld, S., Schmid, B., et al. (2012). Fiji: an open-source platform for biological-image analysis. Nat. Methods *9*, 676–682.

Schirmer, L., Velmeshev, D., Holmqvist, S., Kaufmann, M., Werneburg, S., Jung, D., Vistnes, S., Stockley, J.H., Young, A., Steindel, M., et al. (2019). Neuronal vulnerability and multilineage diversity in multiple sclerosis. Nature *573*, 75–82.

Stassart, R.M., Möbius, W., Nave, K.A., and Edgar, J.M. (2018). The Axon-Myelin Unit in Development and Degenerative Disease. Front. Neurosci. *12*, 467.

Thelen, K.M., Falkai, P., Bayer, T.A., and Lütjohann, D. (2006). Cholesterol synthesis rate in human hippocampus declines with aging. Neurosci. Lett. *403*, 15–19.

Trevisiol, A., Kusch, K., Steyer, A.M., Gregor, I., Nardis, C., Winkler, U., Köhler, S., Restrepo, A., Möbius, W., Werner, H.B., et al. (2020). Structural myelin defects are associated with low axonal ATP levels but rapid recovery from energy deprivation in a mouse model of spastic paraplegia. PLoS Biol. *18*, e3000943.

Vance, J.E., Campenot, R.B., and Vance, D.E. (2000). The synthesis and transport of lipids for axonal growth and nerve regeneration. Biochim. Biophys. Acta *1486*, 84–96.

Voskuhl, R.R., Itoh, N., Tassoni, A., Matsukawa, M.A., Ren, E., Tse, V., Jang, E., Suen, T.T., and Itoh, Y. (2019). Gene expression in oligodendrocytes during remyelination reveals cholesterol homeostasis as a therapeutic target in multiple sclerosis. Proc. Natl. Acad. Sci. USA *116*, 10130–10139.

Wehr, M.C., Laage, R., Bolz, U., Fischer, T.M., Grünewald, S., Scheek, S., Bach, A., Nave, K.A., and Rossner, M.J. (2006). Monitoring regulated protein-protein interactions using split TEV. Nat. Methods *3*, 985–993.

Wickham, H. (2016). ggplot2 - Elegant Graphics for Data Analysis (Springer).

Xu, Q., Bernardo, A., Walker, D., Kanegawa, T., Mahley, R.W., and Huang, Y. (2006). Profile and regulation of apolipoprotein E (ApoE) expression in the CNS in mice with targeting of green fluorescent protein gene to the ApoE locus. J. Neurosci. *26*, 4985–4994.

STAR★METHODS

KEY RESOURCES TABLE

REAGENT or RESOURCE	SOURCE	IDENTIFIER
Antibodies		
ACSA-2	Miltenyi biotec	Cat #130–097-678
BrdU	Biorad	Cat #MCA2483; RRID:AB_808349
CAII	Said Ghandour	RRID:AB_2314062
CD11b	Biolegend	Cat #101201; RRID:AB_312784
CD11b	Miltenyi biotec	Cat #130–093-636
CD3e	Biolegend	Cat #100301; RRID:AB_312666
CD4	Becton Dickinson	Cat #553726; RRID:AB_395010
CD45.2	Biolegend	Cat #109805; RRID:AB_313442
CD8	Becton Dickinson	Cat #550281; RRID:AB_2275792
GFAP	Chemicon	Cat #MAB3402; RRID:AB_94844
IBA1	Wako	Cat #019-19741; RRID:AB_839504
MAC3	Pharmigen	Cat #553322; RRID:AB_394780
MBP	Biorad	Cat #MCA409; RRID:AB_325004
NG2	Merck Millipore	Cat #AB5320; RRID:AB_91789
O4	Miltenyi biotec	Cat #130–096-670; RRID:AB_2847907
Olig2	Prof. Stiles / Dr. Alberta	DF308; RRID:AB_2336877
APP	Sigma	Cat #A8717; RRID:AB_258409
NeuN	Chemicon	Cat# MAB377; RRID:AB_2298772
Chemicals, peptides, and recombinant proteins		
2′,7′-Dichlorofluorescein	Sigma-Aldrich	Cat #D6665
Corn oil	Sigma-Aldrich	Cat #C8267
Cuprizone	Sigma-Aldrich	Cat #14690
Lymphocyteseparation medium	PAA	Cat #LSM1077
M. tuberculosis H37 Ra	BD	Cat #231141
MOG35-55	Max-Planck-Institute (MPI-EM)	N.A.
PageRulerTM	ThermoFisher Scientific	Cat #26619
Pertussis toxin	Sigma-Aldrich	Cat #P7208
Fluoro-Jade C	Sigma-Aldrich	Cat # AG325
Tamoxifen	Sigma-Aldrich	Cat #T5648
Critical commercial assays		
Adult Brain Dissociation Kit	Miltenyi biotec	Cat #130-107-677
DAB Substrate Kit	Zymomed	Cat #DAB057
LSAB®2 System-HRP	Dako	Cat #K0609
Ovation Pico WTA System V2	NuGEN	Cat #3302
RNeasy Mini Kit	QIAGEN	Cat #74104
VECTASTAIN® Elite® ABC HRP Kit	VECTOR	Cat #PK-6100
Deposited data		
GSE118257 Single-nucleus RNA sequencing dataset from white matter areas of post-mortem human brain from patients with Multiple sclerosis and from unaffected controls	(Jäkel et al., 2019)	GEO: GSE118257

(*Continued on next page*)

Continued

REAGENT or RESOURCE	SOURCE	IDENTIFIER
GSE124335 Single-nucleus RNA sequencing dataset assessing changes in the gene expression of multiple cell lineages in Multiple Sclerosis lesions	(Schirmer et al., 2019)	GEO: GSE124335
GSE185092 Microarray (Affymetrix) data of laser-captured callosal projection neurons from WT, CNP-KO and PLP-KO mice at 1, 3, 6, and 12 months of age	This paper	GEO: GSE185092
Experimental models: Organisms/strains		
Plp1-CreERT2	Max-Planck-Institute (MPI-EM)	(Leone et al., 2003)
CSPG4::CreERT2	Max-Planck-Institute (MPI-EM)	(Huang et al., 2014)
GLAST::CreERT2	Max-Planck-Institute (MPI-EM)	(Mori et al., 2006)
CaMKII-Cre	Max-Planck-Institute (MPI-EM)	(Minichiello et al., 1999)
Fdft1$^{flox/flox}$	Max-Planck-Institute (MPI-EM)	(Saher et al., 2005)
Cnp$^{-/-}$ (CNP-KO)	Max-Planck-Institute (MPI-EM)	(Lappe-Siefke et al., 2003)
Plp1$^{-/y}$ (PLP-KO)	ZMBH Heidelberg	(Klugmann et al., 1997)
Thy1-EYFP	ZMBH Heidelberg	(Rossner et al., 2006)
Oligonucleotides		
Primer for RT-qPCR	This paper	N/A
Software and algorithms		
Cytoscape v3.7.1	Otasek et al., 2019	https://cytoscape.org
GraphPad Prism 6	GraphPad Software, Inc.	https://www.graphpad.com/
ImageJ (Fiji)	Schindelin et al., 2012	https://imagej.nih.gov/ij/
InteractiVenn	Heberle et al., 2015	http://www.interactivenn.net/
LAS X software	Leica-microsystems	https://www.leica-microsystems.com
R	This paper	https://www.r-statistik.de
R package ggplot2 v3.2.0	Wickham, 2016	https://cran.r-project.org
R package Seurat v3.1.0	Butler et al., 2018	https://satijalab.org
ZEN 2012 blue edition	Zeiss	https://www.zeiss.de/corporate/home.html

RESOURCE AVAILABILITY

Lead contact

Further information and requests for resources and reagents should be directed to and will be fulfilled by the Lead Contact, Gesine Saher (saher@em.mpg.de).

Materials availability

This study did not generate new unique reagents.

Data and code availability

- This paper analyzes existing, publicly available single-nucleus RNA-seq data. The accession numbers are listed in the Key resources table. Microarray raw data have been deposited at GEO:GSE185092 and are publicly available as of the date of publication.
- This paper does not report original code.
- Any additional information required to reanalyze the data reported in this paper is available from the lead contact upon request.

EXPERIMENTAL MODEL AND SUBJECT DETAILS

All animal studies were performed in compliance with the animal policies of the Max Planck Institute of Experimental Medicine, and were approved by the German Federal State of Lower Saxony. Animals were group-housed (3-5 mice) with 12 h dark/light cycle and

had access to food and water *ad libitum*. Adult male and female C57BL/6N mice (8-10 weeks of age) or cholesterol synthesis mutants (8–10 weeks of age) were taken for all experiments. Male mice were subjected to cuprizone experiments. Female mice were used for non-induced pathology experiments. Animals of same sex were randomly assigned to experimental groups (3-12 mice). Cholesterol synthesis mutants in this study were generated by crossbreeding cell type-specific Cre-driver lines (see Key resources table) with mice harboring squalene synthase floxed mice (*Fdft1*$^{flox/flox}$). Conditional mutants were compared with the respective Cre or homozygous floxed controls, i.e., CaMKII-Cre::*Fdft1*$^{flox/flox}$ mutants and *Fdft1*$^{flox/flox}$ controls, Plp1-CreERT2::*Fdft1*$^{flox/flox}$ mutants and *Fdft1*$^{flox/flox}$ controls, Cspg4/NG2$^{CreERT2/+}$::*Fdft1*$^{flox/flox}$ and Cspg4/NG2$^{CreERT2/+}$ controls, GLAST$^{CreERT2/+}$::*Fdft1*$^{flox/flox}$ mutants and GLAST$^{CreERT2/+}$ controls, Cspg4/NG2$^{CreERT2/+}$::Plp1-CreERT2::*Fdft1*$^{flox/flox}$ mutants and Plp1-CreERT2::*Fdft1*$^{flox/flox}$ and *Fdft1*$^{flox/flox}$ controls. *Cnp* null and *Plp1* null mice were crossbreed to Thy1-EYFPnuc mice to generate CNP mutants (TYNC ±, *Cnp* −/−, *Plp1* +/y) and PLP mutants (TYNC ±, *Cnp* +/+, *Plp1* -/y) that were compared with TYNC ± mice.

METHOD DETAILS

Tamoxifen induced recombination

Transgenic mice received tamoxifen either by oral administration, three times every second day at a concentration of 0.4 mg/g body weight dissolved in corn oil:ethanol (1:9) or by intraperitoneal injections on 5 consecutive days at a concentration of 75 μg/g body weight.

Experimental autoimmune encephalomyelitis (EAE)

MOG-EAE was induced by immunizing subcutaneously with 200 mg myelin oligodendrocyte glycoprotein peptide 35–55 (MOG35–55) in complete Freund's adjuvant (M. tuberculosis at 3.75 mg ml-1) and i.p. injection twice with 500 ng pertussis toxin as described (Berghoff et al., 2017b, 2021). Animals were examined daily and scored for clinical signs of the disease. If disease did not start within 15 days after induction or the clinical score rose above 4, animals were excluded from the analysis. The clinical score was: 0 normal; 0.5 loss of tail tip tone; 1 loss of tail tone; 1.5 ataxia, mild walking deficits (slip off the grid); 2 mild hind limb weakness, severe gait ataxia, twist of the tail causes rotation of the whole body; 2.5 moderate hind limb weakness, cannot grip the grid with hind paw, but able to stay on a upright tilted grid; 3 mild paraparesis, falls down from a upright tiled grid; 3.5 paraparesis of hind limbs (legs strongly affected, but move clearly); 4 paralysis of hind limbs, weakness in forelimbs; 4.5 forelimbs paralyzed; 5 moribund/dead.

Cuprizone

Cuprizone pathology was induced by feeding mice with 0.2% w/w cuprizone (Sigma-Aldrich) in powder chow. Mice received cuprizone for 'acute remyelination' (6 weeks) and 'chronic remyelination' (12 weeks followed by 2 weeks normal chow) paradigms. Chow was replaced three times a week. Age-matched untreated controls were fed powder chow without cuprizone.

Serum Analysis

Blood was collected by cardiac puncture, and serum was prepared after 4 h clotting by centrifugation. Cholesterol measurements were done with the Architect II system (Abbott Diagnostics).

Open field

Exploratory activity in a novel environment was tested in an open field chamber (50x50x50 cm) at 20 lux light intensity. Individual female mice at the age of 22 weeks were placed into left bottom corner of the open field chamber. The exploratory behavior of the mouse was recorded for 10 min using an overhead camera system and scored automatically using the Viewer software (Biobserve, St. Augustin, Germany). The overall traveled distance was analyzed as a parameter of general activity. Time, distance and visits in the center area (25x25 cm) was analyzed to measure behavior related to anxiety. Results were normalized to the mean of corresponding control animals and statistically analyzed using one-way ANOVA with Sidak's post-test.

Blood-brain barrier permeability

Measurements of BBB permeability were done as described (Berghoff et al., 2017a). Tracers were i.v. injected (Evans Blue 50 mg/g body weight, sodium fluorescein 200 mg/g body weight). Animals were flushed with PBS. Brain samples were isolated, weighed, lyophilized at a shelf temperature of –56°C for 24 h under vacuum of 0.2 mBar (Christ LMC-1 BETA 1-16), and extracted with formamide at 57°C for 24 h on a shaker at 300 rpm. Integrated density of tracer fluorescence was determined in triplicates after 1:3 ethanol dilutions to increase sensitivity. Tracer concentration was calculated using a standard curve prepared from tracer spiked brain samples.

Flow cytometry

Single-cell suspensions from spinal cord were obtained via mechanical dissociation on a cell strainer. Immune cells were separated over a two-phase Percoll-density gradient by centrifugation. Staining of CD4+ T cells, CD8+ T cells and CD45/CD11b+ cells (macrophages/microglia) was performed using the following antibodies in a 1:200 dilution: anti-CD3e (clone 145-2C11, BioLegend), anti-CD4 (clone GK 1.5, BD), anti-CD8 (clone 53-6.7, BD), anti-CD11b (clone M1/70, BioLegend), anti-CD45.2 (clone 104, BioLegend).

The addition of CaliBRITE APC beads (BD) allowed for cell quantification. Flow cytometry was performed using a CytoFLEX S (Beckman Coulter) operated by CytExpert software (Beckman Coulter, v2.4).

Magnetic cell isolation (MACS)

Glial cells and neurons were isolated according to the adult brain dissociation protocol (Miltenyi biotec) form corpus callosum and/or cortex. Antibody labeling was done according to the Microbead kit protocols (Miltenyi biotec) for oligodendrocytes (O4) or astrocytes (ACSA-2). Neurons were isolated by negative selection. Purity of cell populations was routinely determined by RT-qPCR on extracted and reverse transcribed RNA.

Expression analyses

For expression analyses of tissue samples, mice were killed by cervical dislocation. Samples were quickly cooled and region of interest prepared. RNA was extracted using RNeasy Mini kit (QIAGEN). cDNA was synthesized with Superscript III (Invitrogen). Concentration and quality of RNA was evaluated using a NanoDrop spectrophotometer and RNA Nano (Agilent). RNA from MACS-purified cells was extracted using QIAshredder and RNeasy protocols (QIAGEN). cDNA was amplified by Single Primer Isothermal Amplification (Ribo-SPIA® technology) using Ovation PicoSL WTA System V2 (NuGEN) following the manufactures protocol. Quantitative PCRs were done in triplicates using the GoTaq qPCR Master Mix (Promega, A6002) and the LightCycler 480 Instrument (Roche Diagnostics). Expression values were normalized to the mean of housekeeping genes. Quantification was done by applying the ΔΔCt method, normalized to experimental controls (set to 1). All primers (Table S1) were designed to fulfill optimal criteria e.g., length (18-22 bp), melting temperature (52-58°C), GC content (40%–60%), low number of repeats, and amplicon length (< 220 bp). All primers were intron-spanning.

Histochemistry

Mice were perfused with 4% formaldehyde (PFA). In case of cuprizone treated animals, brain samples were cut at Bregma 1.58 to account for regional specificity of cuprizone pathology. Tissue was postfixed overnight, embedded in paraffin and cut into 5 μm sections (HMP 110, MICROM). For Gallyas silver impregnation, deparaffinized sections were incubated with a 2:1 mixture of pyridine and acetic anhydride for 30 min at room temperature (RT) to minimize background and increase myelin. Tissue was washed with ddH_20, following heating in incubation solution (0.1% [w/v] ammonium nitrate, 0.1% [w/v] silver nitrate, 12‰ [w/v] sodium hydroxide pH 7.5) for 1 min (100 W) and further incubation for 10 min at RT. After washing with 0.5% [v/v] acetic acid three times for 5 min, sections were incubated in developer solution for 3-10 min. For reconstitution of the developer, 70 mL of solution B (0.2% [w/v] ammonium nitrate, 0.2% [w/v] silver nitrate, 1% [w/v] wolframosilicic acid) was added to 100 mL of solution A (5% [w/v] sodium carbonate) with constant and gentle shaking and then slowly added to 30ml solution C (0.2% [w/v] ammonium nitrate, 0.2% [w/v] silver nitrate, 1% [w/v] wolframosilicic acid, 0.26% [w/v] PFA). The reaction was stopped and fixed by washing in 1.0% [v/v] acetic acid and 2% [v/v] sodium thiosulfate. Tissue was dehydrated and mounted using Eukitt. For detection of apoptotic cells, a TUNEL assay was done according to the manufacturer (Promega G7130). Fluoro-Jade C staining (Sigma, AG 325) was done according to the manufacturers' instructions. Immunohistological stainings were done on deparaffinized sections followed by antigen-retrieval in sodium citrate buffer (0.01 M, pH 6.0). For chromogenic stainings, blocking of endogenous peroxidase activity with 3% hydrogen peroxide was performed followed by 20% goat serum block and incubation with primary antibodies. Detection was carried out with the LSAB2 System-HRP (anti-rabbit/mouse LSAB2 Kit Dako Cat#K0679, dilution 1:100) or the VECTASTAIN Elite ABC HRP Kit (Vector Labs, Anti-Rat IgG Vector Cat#BA-9400, dilution 1:100). HRP substrate 3,30-diaminobenzidine (DAB) was applied by using the DAB Zytomed Kit (Zytomed Systems GmbH). Nuclear labeling was done by hematoxylin stain. For immunofluorescence detection, blocking was performed with serum-free protein block (Dako). Primary antibodies were diluted in 2% bovine serum albumin (BSA)/PBS and incubated for 48 h followed by incubation with fluorophore-coupled secondary antibodies (Alexa488 donkey anti-mouse Invitrogen Cat #A-21202, dilution 1:1000; Alexa488 donkey anti-rabbit Invitrogen Cat #A-21206,dilution 1:1000; Alexa555 donkey anti-rabbit Invitrogen Cat #A-31572, dilution 1:1000). Stained sections were analyzed on an Axio Imager.Z1 (Zeiss) equipped with an AxioCam MRc3, x0.63 Camera Adaptor and the ZEN 2012 blue edition software using 10x objective (Plan Apochromat x10/0.45 M27) or 20x objective (Plan-Apochromat x20/0.8) and evaluated with ImageJ software. Quantification of areas (Gallyas, GFAP, MAC3) were done by applying semi-automated ImageJ software macro including thresholding and color deconvolution. Two to four sections per animal were analyzed.

Quantification of sterols

Sterol abundance was quantified by lipid gas chromatography coupled to mass spectrometry (GC-MS) in acutely isolated neurons and tissue samples (4-5 animals grouped for each replicate). Samples were lyophilized at a shelf temperature of –56°C for 24 h under vacuum of 0.2 millibars (Christ LMC-1 BETA 1-16) and weighed for the calculation of water content and normalization. Metabolites were extracted in a two-phase system of 3:1 methyl-tert-butyl ether:methanol (vol/vol) and water, and pentadecanoic acid was added as an internal standard. The organic phase (10–200 μl) was dried under a stream of nitrogen, dissolved in 10–15 μL pyridine and derivatized with twice the volume of N-methyl-N-(trimethylsilyl) trifluoroacetamide (MSTFA) to transform the sterols and the standard to their trimethylsilyl (TMS) derivatives. Each sample was analyzed twice, with a higher split to quantify cholesterol and with a lower split to measure all other sterols. The samples were analyzed on an Agilent 5977N mass-selective detector connected to an

Agilent 7890B gas chromatograph equipped with a capillary HP5-MS column (30 m × 0.25 mm; 0.25-μm coating thickness; J&W Scientific, Agilent). Helium was used as a carrier gas (1 mL/min). The inlet temperature was set to 280°C, and the temperature gradient applied was 180°C for 1 min, 180–320°C at 5 K min–1 and 320°C for 5 min. Electron energy of 70 eV, an ion source temperature of 230°C and a transfer line temperature of 280°C were used. Spectra were recorded in the range of 70–600 Da/e (ChemStation Software D.01.02.16). Sterols were identified by the use of external standards.

Light sheet microscopy

PFA immersion fixed spinal cord segments were processed for whole mount immune-labeling and tissue clearing following a modified iDISCO protocol (Berghoff et al., 2021). Briefly, samples were dehydrated in ascending methanol (MeOH)/PBS series followed by overnight bleaching /permeabilization in a mix of 5% H_2O_2/20% DMSO/MeOH at 4°C. Samples were further washed in MeOH and incubated in 20% DMSO/MeOH at RT for 2 h. Then, samples were rehydrated using a descending methanol/PBS series and further washed with in PBS/0.2% Triton X-100 for 2 h. The samples were then incubated overnight in 0.2% Triton X-100, 20% DMSO, and 0.3 M glycine in PBS at 37°C and blocked using PBS containing 6% goat serum, 10% DMSO and 0.2% Triton X-100 for 2 days at 37°C. Samples were retrieved, washed twice in PBS containing 0.2% Tween20 and 10μg/mL heparin (PTwH) and incubated with primary antibody solution (Iba1 1:500; PTwH/5%DMSO/3% goat serum) for 7 days at 37°C. After several washes, samples were incubated with secondary antibody solution (1:500 in PTwH/3% goat serum) for 4 days at 37°C. Prior to clearing, the samples were washed in PTwH and embedded in 2% Phytagel (Sigma Aldrich #P8169) in water. The embedded tissue was then dehydrated using an ascending series of Methanol/PBS and incubated overnight incubation in a mixture of 33% dichloromethan (DCM) and 66% MeOH at RT. Samples were further delipidated by incubation in 100% DCM for 40min and transferred to pure ethyl cinnamate (Eci; Sigma Aldrich #112372) as clearing reagent. Tissues became transparent after 15min in Eci and were stored at RT until imaging. Light sheet microscopy was performed using a LaVision Ultramicroscope II equipped with 2x objective, corrected dipping cap and zoom body. Spinal cords were mounted onto the sample holder with the dorsal/ventral axis facing down (z imaging axis = dorsoventral axis spinal cord). The holder was placed into the imaging chamber filled with Eci. Images were acquired in 3D multicolor mode with the following specifications: 5μm sheet thickness; 40% sheet width; 2x zoom; 4μm z-step size; one site sheet illumination; 100ms camera exposure time; full field of view. Autofluorescence was recorded using 488nm laser excitation (80% laser power) and a 525/40 emmision filter and red fluorescence was recorded using 561nm laser excitation (30% laser power) and 585/40 emission filters. Images were loaded into Vision4D 3.0 (Arivis) and the image set was cropped to 500 - 2000 pixels corresponding to 2.2 mm of spinal cord length. The volume of the spinal cord was determined by performing an automatic intensity thresholding on the autofluorescence channel. Phagocytes were detected by running a manual intensity thresholding on the 561nm channel and Iba1 cell accumulation with a volume of < 1000μm3 was considered lesion positive. Then total lesion volume as well as the lesion volume fraction in respect to the total spinal cord volume were calculated. For 3D rendering, the autofluorescence and Iba1 channel were depicted in green and red pseudocolor, respectively. High-resolution images as well as the Video S1 were created using the Arivis 4D viewer.

Laser capture microdissection

Serial cryostat coronal brain sections at the level of Bregma 1 mm to 0.5 mm were prepared (Leica) for single cell isolation). 700 and 800 EYFP+ neurons for each individual sample were microdissected (Arcturus Veritas microdissection system with fluorescence package) from the motor and somatosensory cortex and captured in HS Transfer Cap (Molecular Devices). Cells were only collected if no adjacent nuclei were detected in close proximity. Successful cutting and collection steps were subsequently validated in bright-field and fluorescent mode on the quality control slot of the device. Microdissected cells were lysed in 100 μl of RNA lysis buffer (QIAGEN, Hilden, Germany) and stored at −80°C until further use. All procedures were done under RNase-free conditions.

Microarray expression analysis

Total RNA of pooled single cells was resuspended with pretested T7-tagged dT21V oligonucleotides. Two-round T7-RNA polymerase-mediated linear amplification was performed according to optimized protocols for low-input RNA amounts (Small Sample Target Labeling Assay Version II, Affymetrix). Biotin-labeled second-round aRNA was generated with an NTP-mix containing Biotin-11-CTP and Biotin-16-UTP (PerkinElmer, Boston, MA) at 2 mM. Biotin-labeled amplified RNA (aRNA) size distribution and quantity was analyzed with the Agilent 2100 Bioanalyser using the RNA 6000 Nano LabChip kit (Agilent Technologies, Boeblingen, Germany). Samples with lower size compressed RNA products were discarded. At least 5 μg of labeled cRNA was fragmented by heating the sample to 95°C for 35 min in a volume of 20 μl containing 40 mM Tris acetate pH 8.1, 100 mM KOAc, and 30 mM MgOAc. Fragmentation was checked by alkaline agarose electrophoresis. Hybridization, washing, staining, and scanning were performed under standard conditions as described by the manufacturer. Mouse430A 2.0 genechips were used that contain over 22,600 probe sets representing transcripts and variants from over 14,000 mouse genes. Microarray raw data were exported using Gene chip operating software (Affymetrix). Normalization and higher-level analysis were done in R (for packages see Key resources table). Normalization was carried out using the Robust Multichip Average (RMA) model implemented in the R package Affy at default settings. The normalized microarray data was quality controlled (box-plot analysis, principal component analysis, and Spearman correlation tree) which led to the exclusion of two microarrays. The remaining data were re-normalized, log transformed and filtered based on absolute expression values (100 fold changed signal intensity cutoff). Probe sets with a fold change higher than 1.5 were included in further analysis for single gene analysis. A fold change threshold of 1.3 was applied for further pathway level analysis using gene

set enrichment analysis (GSEA; https://www.gsea-msigdb.org/gsea/index.jsp). GSEA was performed with 5214 different gene sets obtained from Molecular Signature Database (MSigDB) at the Broad Institute (MIT).

Human single-nuclei transcriptome sequencing datasets

Human single-nuclei RNA sequencing profiles were obtained from two available datasets, GSE118257 (Jäkel et al., 2019) and GSE124335 (Schirmer et al., 2019), and re-analyzed by R package Seurat v3.2.3. Both datasets were filtered and embedded according to parameters of original publications. Annotations of neurons, oligodendrocytes, and astrocytes were confirmed using marker gene expression of the different cell types (Figure S3). Subsequently, gene counts from neuron, oligodendrocyte and astrocyte subsets from both datasets were merged by applying Canonical Correlation Analysis (CCA) integration method. Uniform Manifold Approximation and Projection (UMAP) was used to visualize cell merging results. For each cell type, pairwise comparisons (MS lesion versus control and MS non-lesion versus control) of expression of genes related to cholesterol synthesis and metabolism were computed using normalized gene counts by Model-based Analysis of Single-cell Transcriptomics (MAST) R package v.1.12.0. Heatmap visualization was computed using R package pheatmap v.1.0.12 (Pretty Heatmaps).

Spinal cord co-cultures

Spinal cord co-cultures were established as described (Bijland et al., 2019) from embryonic day 13 mouse embryos. Cells were plated initially in 12.5% horse serum and fed the following day and every second or third day thereafter with serum-free differentiation medium. On day *in vitro* (DIV) 14 (before myelination commences around DIV 17), cultures were treated with cholesterol (10 μg/mL), cholesterol and tetrodotoxin (TTX) (1μM, Tocris), or 0.1% ethanol (vehicle control) for 3 days. On DIV 17, bromodeoxyuridine (BrdU; 10 μM) was added to the cultures for 2 h. Cultures were fixed with PFA and washed in PBS. Cells were permeabilized for 10 min in 0.5% Triton X in PBS and incubated for 48 h at 4°C in rabbit anti-NG2 (AB5320, Merck Millipore; 1:500) and rat anti-MBP (MCA409, Biorad, 1:500) in 10% goat serum, 1% bovine serum albumin in PBS. Following application of Alexa 596 anti-rabbit IgG and Alexa 488 anti-rat IgG (Invitrogen, 1:1000 for 1 h), cells were fixed in 50:50 acetic acid and ethanol for 10 min and DNA was denatured in 2M HCl for 30 min. Then anti-BrdU (MCA2483T, Biorad; 1:500) was added in blocking buffer and incubated overnight. Alexa 647 anti-mouse IgG1 (Invitrogen, 1:1000) was added for ~1 h at room temperature and coverslips were mounted in Mowiol with DAPI (2.5 μg/mL). 10 predefined locations were selected in the DAPI channel, and images were captured at 10x magnification using a Zeiss Axio Imager M.2 with an AxioCam MRm. Analysis of MBP positive area was performed by automated thresholding (Triangle, ImageJ). Quantification of the number of NG2 and BrdU double positive cells was done on binarized images and normalized to the DAPI-positive cell density with the particle analyzer plugin (ImageJ).

Whole cell current clamp and microelectrode arrays

Whole cell patch clamp recording was performed on DIV 21 cultures using an Axopatch 200B amplifier with a Digidata 1440A digital acquisition system and pClamp 10 software (Molecular Devices). Experiments were performed at 37°C in atmospheric air using an extracellular solution containing (in mM): 144 NaCl, 5.3 KCl, 2.5 $CaCl_2$, 1 $MgCl_2$, 10 HEPES, 10 mM glucose, pH 7.4. The pipette solution contained (in mM): 130 mM K^+ gluconate, 4 mM NaCl, 0.5 mM $CaCl_2$, 10 mM HEPES, 0.5 EGTA pH 7.2. Borosilicate glass pipettes were pulled to a resistance of 3-8 MΩ. Liquid junction potentials were measured as 20 mV and traces were offset by this value. For microelectrode arrays, cultures were plated and maintained on commercial MEAs (60MEA200/30iR-Ti-gr; Multi Channel Systems, Reutlingen, Germany) as described previously (Bijland et al., 2019). A fluorinated ethylene-propylene membrane (ALA MEA-MEM-SHEET) sealed the MEA culture dishes. The recordings were done in differentiation medium. Signals were digitally filtered at 3 Hz high pass filter, 1 kHz low pass filter and amplified up to x20,000. A digital notch filter was used to remove 60 Hz noise during recording. For data acquisition and analysis, spikes and potentials were sorted and counted from 3-min gap-free recordings using the pCLAMP10 software (Molecular Devices Corporation, California, USA).

QUANTIFICATION AND STATISTICAL ANALYSIS

Number of animals for each experiment is provided in the figure legends. No statistical methods were used to pre-determine sample sizes but our sample sizes are similar to those reported in previous publications (Berghoff et al., 2021). No inclusion or exclusion criteria were used if not otherwise stated. Studies were conducted blinded to investigators and/or formally randomized. Data are expressed as mean with individual data points unless otherwise indicated. For statistical analysis, unpaired two-sided Student's t test, one-way ANOVA or two-way ANOVA with Sidak's or Tukey's post tests were applied. Normality was tested by using the Kolmogorov-Smirnov test. If the n was below 5, we assumed normal distribution. "Signal-to-Noise ratio" (SNR) statistics were used to rank genes for GSEA of microarray data. Linear model fitting and subsequent testing for differential expression by empirical Bayes variance moderation method implemented in R packaged limma v3.42.2 was applied to the 6-month neuron microarray data. Wilcoxon Rans Sum test was used for analysis of snRNaseq data material. Data analysis was performed using GraphPad Prism Software Version 6 (GraphPad) and the R software. A value of $p < 0.05$ was considered statistically significant. Asterisks depict statistically significant differences (* $p < 0.05$, ** $p < 0.01$, *** $p < 0.001$).